Ionospheric Disturbances in Mexican Territory Produced by Objects Entering the Atmosphere from Space

February 11, 2022

Abstract

Earth's ionosphere may be perturbed by different phenomena, such as geomagnetic storms, solar flares with a common origin in our star, the Sun. In this work we will study the effects in the ionosphere caused by objects coming from outside the atmosphere (asteroids) inside Mexican territory. The Geostationary Lightning Mapper (GLM) started to record the passage of fireballs since 2017 and has recorded over 3000 events in the American continent. By the other hand, the Center for Near Earth Object Studies has data of 886 meteors detected around the globe by the United States Government sensors (USG). From these databases, we chose a sample of events and collected data and estimated meteor properties such as mass and energy released (if not available). Also we collected GPS data from UNAVCO network for the days each event was reported looking for vestiges of the meteors passage. With this work, we have observed that the vTEC signal of the ionosphere observed and calculated with GPS data from stations on Earth, is affected by the passage of these objects producing ionospheric perturbations with a permanence of a twice hours in average.

1 Introduction

The Earth's magnetic field represents a final obstacle to the Solar Wind (SW) flux. When decelerated and defected by a non colisional shock wave in the flux direction, generates a cavity known as magnetosphere (Blanco-Cano et al., 2004). Since the Earth is embedded in this SW flux, is known that under adequate physical conditions (e.g magnetic reconnection) may exist some coupling between the magnetosphere and the Earth's ionosphere (Zolesi & Cander, 2014; Cnossen et al., 2012).

The Sun plays an important role in the physical processes that occur in the terrestrial magnetosphere-ionosphere system. When the SW interacts with the Earth's magnetosphere, particles may permeate the internal region via magnetic reconnection and penetrate to polar zones and generate boreal or austral auroras thus altering the system (Vázquez et al., 2016; Oka et al., 2011). By the other hand, the Extreme Ultraviolet Radiation (EUV) and X-rays coming from the Sun may interact with the neutral atmoshere via photoionization (Vlasov & Kelley, 2010). However, in both cases the final result is that the ionosphere's free electrons population is altered.

Some Ionospheric Perturbations (IP) become relevant due to their spatial and temporal scale in the Space Weather scenario. At intermediate latitudes, the most common in the ionosphere are known as Traveling Ionospheric Disturbances (TIDs). Typically they divide into two groups: a) large scale TIDs, associated with geomagnetic storms with sizes of $\sim$2000 km, periods of $\sim$1 h and velocities of $\sim$700 km s^{-1}, and b) Medium-scale TIDs, which are not fully associated with geomagnetic storms, present sizes of $\sim$100 km, periods from 10 minutes to 1 hour and velocities between 50 km s^{-1} and 1×10^2 km s^{-1} (Helmboldt et al., 2012). Diverse methods have benn used to study TIDs, such as incoherent dispersion radars, high frequency Doppler emmisors, data from Global Positioning System (GPS) stations or even radiotelescopes like the VLA or the Mexican Array Radio Telescope (MEXART) (Chilcote et al., 2015; Rodríguez-Martínez et al., 2014).

On the other side, the Earth's ionosphere may be affected or modified by other proccesses, particularly there are studies that show how the Vetical Total Electron Content (vTEC) due to shock waves generated for rockets launched to space (Lin et al., 2014). Similar proccesses modify the Earth's ionosphere due to objects entering the athmosphere from space, such as meteoroids like the one which fell on Chelyabinsk at 2013 (Yang et al., 2014). Previously, the ionospheric perturbations produced by this object were studied using two independent methods: a) detecting vTEC pertubations using GPS station near the impact location. And b) a wavelets analysis for detection of ...

In 2020 a meteoroid passed in mexican territory through mexican territory, which also was studied (Sergeeva et al., 2021). The meteoroid was recorded with outdoor cameras in different locations. The trajectory could be estimated, as well as other physical parameters.

In this work we will show a similar analysis for a sample of meteoroids detected in Mexican territory by different methods. The first subsample consists in objects detected by the Geostationary Lightning Mapper (GLM) whose sizes are estimated between a few decimeters to meters in diameter (Goodman et al., 2013; Jenniskens et al., 2018; Rumpf et al., 2019). The second subsample will consist in objects detected by ocular witnesses from the American Meteor Society and as comparisson we will include the morelian meteoroid reported in Sergeeva et al. (2021) and the Chelyabinsk event Yang et al. (2014). The paper is arranged in the following way: §2 describes the samples of meteoroids as well of the properties that can be obtained from direct observations. Also describes the GPS data corresponding to the dates and locations where each object was located. §3 shows physical parameters of meteoroids obtained from the observed heights and energies. Finally, section §4 shows the vTEC maps and scintillation indices obtained from GPS observations.

2 Observational data

2.1 Meteors Databases

We selected a sample of meteors which were observed in mexican territory from the Geostationary Lightning Mapper (Goodman et al., 2013). Originally this project was designed to detect lightning activity in earth's atmosphere, but has been proven that also can detect bolides entering the atmosphere. The detection comes from two satellites called GOES-16 and GOES-17 orbiting the earth in geostationary orbits. We used the interactive database

available at `https://neo-bolide.ndc.nasa.gov/#/`. These data are publicly available and easily downloaded from the same website. For each event we can obtain the recorded trajectory of meteors and the corresponding light curve. The GLM satellites have an umbral magnitude for detection of -14. At this magnitude, a meteor is considered a bolide, and is expected to be at least decimeter-sized (in diameter) to reach such brightness. In the other hand, too bright meteors will saturate the detectors, and thus, lowering the quality of data. The result of this factors implies that the range in size of the objects in our sample should vary in diameter between decimeter to meter size. Each event also has assigned a confidence ratio, from low confidence to high, depending in how bright is the event itself and if the trajectory recorded by GLM ressembles a straight line. We chose only events whose confidence ratio is high, in order to be sure we chose the brightest objects, and thus, in the diameter size of bolides, we favored the meter-sized ones. In table 1 we list the object we chose to do this work, order in chronological order. GOES-16 and GOES-17 systematically detect the meteors at slightly different positions and at slightly different times, so we calculated the mean of the duration, latitude and longitude reported by both satellites for each event, and used the standard deviation as the uncertainties. In figure 1 we show the actual positions at which each bolide was detected.

From table 1 is also clear that the duration of all the bolides detection last less than a second. This observation suggests that the bolides remain undetected by the GLM satellites until they get fragmented due to stagnation pressure when they release a huge amount of energy and thus they become detectable.

By the other hand, we got another sample of 10 bolides from US Goverment (USG) sensors from the Center for Near Earth Object Studies (CNEOS), publicly available at `https://cneos.jpl.nasa.gov/fireballs/`, where we may obtain directly data about bolides position, the date and time each bolide was detected, the energy released at fragmentation, the velocity and the height (the last two not available for all bolides). As seen in table 2, the time span is quite larger, and the released energy is generally larger. Some elements appear in both samples, since are bright enough to be detected regardless the project involved. In USG sample, the total energy of each meteor is already available from the database, but the energy for GLM bolides needs to be estimated. To do so, we estimated the distance between GOES satellites and the bolide and then followed Jenniskens et al. (2018), but we find some discrepancies in our measurements repect what is already reported for the same bolides in the USG database. (see the appendix A and B) for more details. We assumed that such discrepancy is due that GLM detectors underestimate the radiated energy by the bolides since before fragmentation the bolides remain undetectable by GLM sensors, and thus a fraction of the radiated energy is not accounted. To solve this, we estimated a correction factor using the bolides that appears in both GLM and USG samples (see figure 7 in appendix B). The energy distributions of USG and GLM samples are compared directly in figure 2.

2.2 GPS data

We got RINEX data from 3 to 7 stations depending of the event location and data availability that surround the event place in all directions as possible. A list of the stations where we got RINEX data is available in table. Most of the stations lie in mexican territory, but in some cases we required data from other stations to cover events near the mexican frontier at

Table 1: List of bolides detected in mexican territory (plus one detected near Venezuela and one detected near Cuba), detected by the Geostationary Lighning mapper. The events are listed in chronological order. The listed duration, latitude and longitude correspond to the mean of the measurements of both GOES satellites. The uncertainties correspond to the respecting mean deviation.

| ID	Date of event	Start Time (UT)	Duration (seconds)	Latitude (deg)	Longitude (deg)	Altitude (km)
GLM-00	2019-02-01	18:17:09	2.651 ± 0.4907	22.45 ± 0.071	-83.50 ± 0.424	24
GLM-01	2019-05-23	16:36:18	0.197 ± 0.0000	24.30 ± 0.000	-101.60 ± 0.849	28
GLM-02	2019-07-18	14:30:30	0.058 ± 0.0000	27.20 ± 0.000	-103.15 ± 0.778	72
GLM-03	2019-08-10	11:18:48	0.199 ± 0.0757	21.50 ± 0.000	-102.50 ± 0.849	92
GLM-04	2019-10-03	07:55:33	0.106 ± 0.0297	25.65 ± 0.071	-96.25 ± 0.778	74
GLM-05	2019-10-09	06:08:11	0.103 ± 0.0078	23.60 ± 0.000	-111.95 ± 0.212	32
GLM-06	2019-11-16	09:36:04	0.396 ± 0.0134	20.30 ± 0.000	-100.55 ± 0.919	82
GLM-07	2019-11-17	15:36:01	0.116 ± 0.0035	31.70 ± 0.000	-117.70 ± 1.131	88
GLM-08	2019-11-19	07:57:40	0.097 ± 0.1138	20.00 ± 0.000	-88.40 ± 1.131	99
GLM-09	2019-11-26	13:23:20	0.078 ± 0.0290	23.90 ± 0.000	-108.70 ± 0.849	81
GLM-10	2019-12-04	09:42:54	0.173 ± 0.0028	31.50 ± 0.000	-113.65 ± 0.919	77
GLM-11	2019-12-15	14:50:49	0.127 ± 0.0134	27.70 ± 0.000	-114.10 ± 0.849	78
GLM-12	2019-12-29	16:16:35	0.062 ± 0.0134	29.60 ± 0.000	-116.35 ± 0.919	79
GLM-13	2020-01-03	14:10:17	0.113 ± 0.0085	30.20 ± 0.000	-117.65 ± 0.919	74
GLM-14	2020-01-06	16:39:27	0.118 ± 0.0042	31.40 ± 0.000	-108.20 ± 0.990	81
GLM-15	2020-01-15	15:00:33	0.213 ± 0.1351	19.45 ± 0.071	-95.55 ± 0.919	93
GLM-16	2020-02-12	09:25:40	0.210 ± 0.0226	18.90 ± 0.000	-93.50 ± 0.849	90
GLM-17	2020-03-03	12:33:27	0.062 ± 0.0007	18.25 ± 0.071	-106.35 ± 0.636	77
GLM-18	2020-03-31	19:31:52	0.105 ± 0.0573	28.45 ± 0.071	-112.05 ± 0.636	61
GLM-19	2020-04-08	16:25:28	0.120 ± 0.0926	26.10 ± 0.000	-93.90 ± 0.849	78
GLM-20	2020-04-18	17:43:25	0.139 ± 0.0106	29.00 ± 0.000	-106.55 ± 0.919	82
GLM-21	2020-04-20	16:05:22	0.318 ± 0.1655	28.15 ± 0.071	-97.85 ± 1.061	88
GLM-22	2020-04-25	11:03:09	0.323 ± 0.0813	32.15 ± 0.071	-111.60 ± 1.131	84
GLM-23	2020-04-28	19:31:52	0.105 ± 0.0573	28.45 ± 0.071	-112.05 ± 0.636	29
GLM-24	2020-05-08	10:06:16	0.490 ± 0.0750	21.60 ± 0.000	-92.40 ± 0.849	81
GLM-25	2020-07-15	19:58:28	0.693 ± 0.0495	24.00 ± 0.000	-108.35 ± 0.495	53
GLM-26	2020-08-07	13:29:57	0.163 ± 0.0057	28.80 ± 0.000	-106.05 ± 0.919	89
GLM-27	2020-09-13	16:41:59	0.184 ± 0.0078	28.45 ± 0.071	-113.75 ± 0.919	85
GLM-28	2020-09-30	12:28:11	0.100 ± 0.0078	24.90 ± 0.000	-110.90 ± 0.849	83
GLM-29	2020-11-16	12:28:11	0.100 ± 0.0078	24.90 ± 0.000	-110.90 ± 0.849	106
GLM-30	2020-11-17	12:53:41	0.404 ± 0.0262	23.00 ± 0.000	-102.45 ± 0.919	93
GLM-31	2020-12-19	10:18:14	0.407 ± 0.0110	21.95 ± 0.071	-101.60 ± 0.990	98
GLM-32	2020-12-23	09:43:01	0.148 ± 0.0014	25.75 ± 0.071	-111.25 ± 0.778	81
GLM-33	2020-12-29	15:20:54	0.118 ± 0.0014	16.80 ± 0.000	-102.20 ± 0.707	81
GLM-34	2021-03-31	09:01:17	0.753 ± 0.3083	20.15 ± 0.071	-92.95 ± 0.212	24
GLM-Ven	2019-06-22	21:25:45	4.873 ± 0.0000	14.9 ± 0.000	-65.8 ± 0.000	25
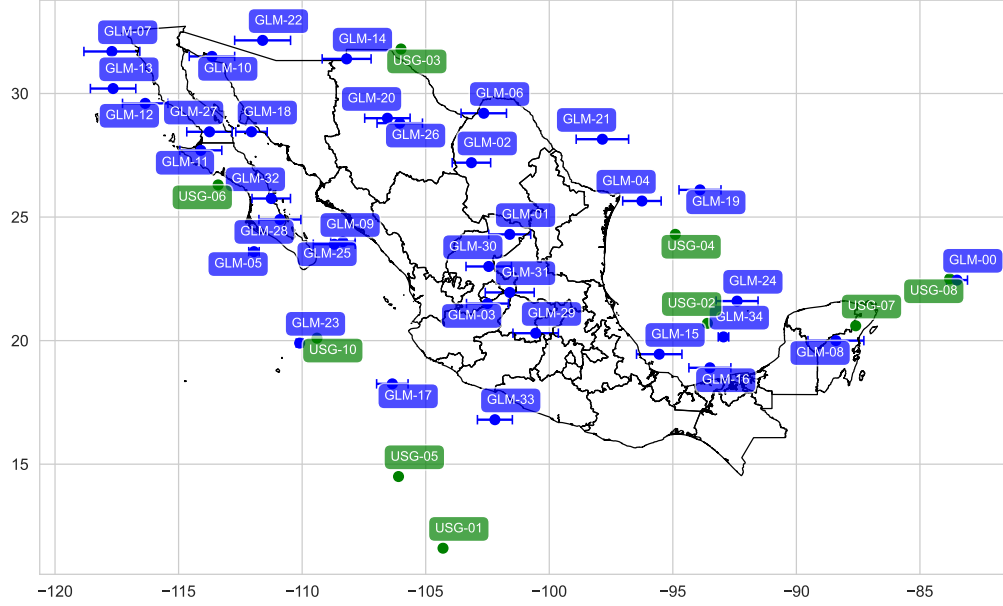
Figure 1: Positions of events from table 1 (blue) and table 2. The events GLM-00/USG-08 actually correpond to the same bolide, but there are little discrepancies about the position where the bolide was detected. The same applies for the events GLM-23/USG-10 and GLM-Ven/USG-09, which not appears in the map.

Table 2: List of bolides detected in mexican territory (plus one detected near Venezuela and one detected near Cuba), detected by USG sensors.

ID	Date of event	Start Time (UT)	Velocity (km/s)				Latitude (deg)	Longitude (deg)	Altitude (km)
			v	v_x	v_y	v_z			
USG-01	1995-08-05	17:14:10					11.6	-104.3	
USG-02	1996-07-12	14:04:45					20.7	-93.6	
USG-03	1997-10-09	18:47:15					31.8	-106.0	37.0
USG-04	2000-01-18	08:33:58					24.3	-94.9	
USG-05	2000-08-25	01:12:25					14.5	-106.1	
USG-06	2005-11-15	05:19:07					26.3	-113.4	32.4
USG-07	2015-07-19	07:06:26	17.8	9.4	13.0	7.8	20.6	-87.6	22.0
USG-08	2019-02-01	18:17:10	16.3	-2.4	13.6	8.7	22.5	-83.8	23.7
USG-09	2019-06-22	21:25:48	14.9	-13.4	6.0	2.5	14.9	-66.2	25.0
USG-10	2020-04-28	05:43:17					20.1	-109.4	
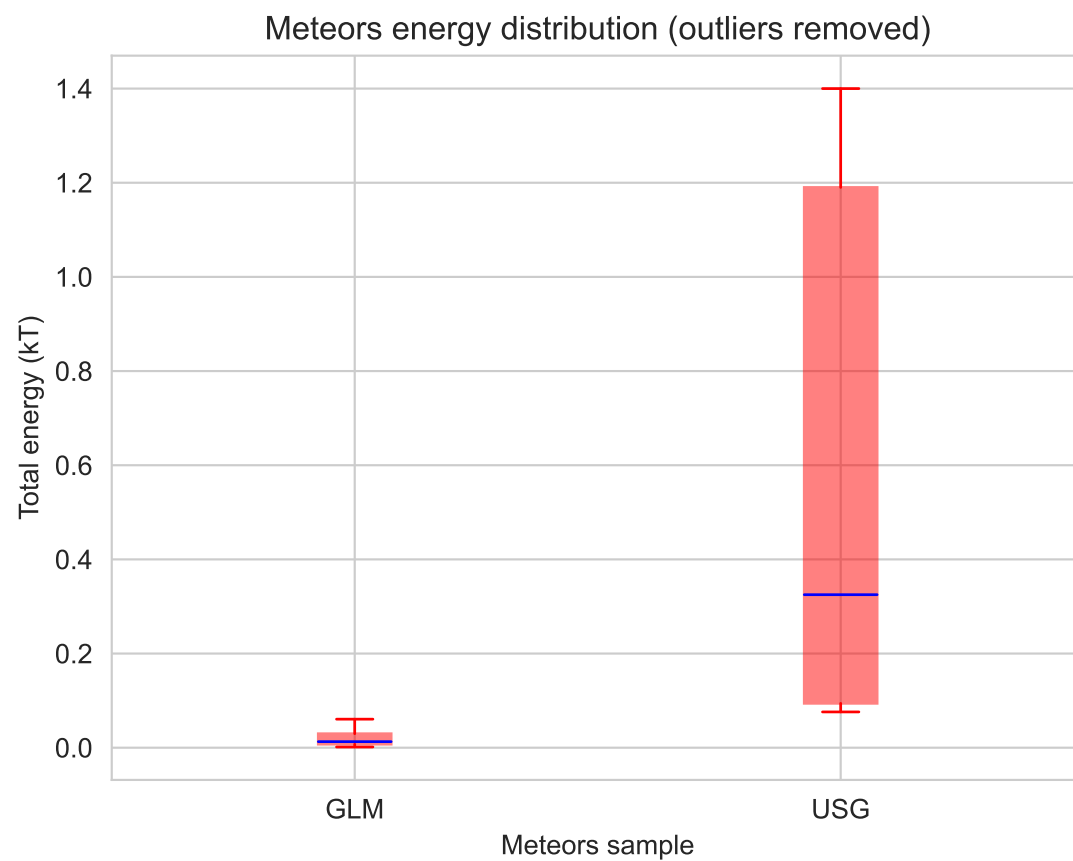
Figure 2: Comparison between released energies of bolides detected by the Geostationary Lightning Mapper and USG sensors.

north or south.

The obtained RINEX files are compressed in Hatanaka format, developed at the Geographical Survey Institute by Y. Hatanaka (Kumar et al., 2012). From this files we may estimate the Slant Total Electron Content (sTEC) and the Vertical Total Electron Content (vTEC) which may be computed in the following way:

The Total Electron content along the integrated path of the link (s_i) at the frequency f_i can be inferred from the phase delay L_i of the frequency f_i (Emery & Camps, 2017):

$$L_i = s_i - \frac{40.3082\,\mathrm{m^3\,s^{-1}}}{f_i^2} sTEC_i \tag{1}$$

Combining two observations at two different frequencies f_1 and f_2 we may obtain two different phase delays L_1 and L_2 and derive the TEC along the signal path:

$$sTEC = \frac{f_1^2 f_2^2 (L_1 - L_2)}{40.3082\,\mathrm{m^3\,s^{-1}}\,(f_1^2 - f_2^2)} \tag{2}$$

In the other hand, the Vertical Total Electron Content (vTEC) is computed from the sTEC as follows (Kumar et al., 2012):

$$vTEC = \frac{sTEC - [b_R + b_S]}{S(\theta_I)} \tag{3}$$

where b_R and b_S are receiver and satellite biases, respectively. θ_I is the elevation angle in degrees, $S(\theta_I)$ is the obliquity factor with zenith angle ψ at the Ionospheric Pierce Point (IPP):

$$S(\theta_i) = \frac{1}{\cos\psi} = \left\{ 1 - \frac{R_E \cos\theta_I}{R_E + h} \right\}^{-1/2} \tag{4}$$

Where R_E is the Earth radius in km and $h = 350\,\mathrm{km}$ is the ionospheric shell above the earth's surface.

Using a software developed by Gopi K. Seemala, publicly available at `https://seemala.blogspot.com/`, we computed the slant TEC (TEC) and vertical TEC (vTEC) for a several number of GPS satellites, each one identified with a PseudoRandom Noise code (PRN). An example of such TEC calculations is shown in figure 2.2. The behavior of the TEC curve is due to many factors, including the earth's rotation, solar activity, etc. TID's and wave-like features are not as prominent and are difficult to see. So we focused in a time interval close to the moment the bolide was detected, and detrended our time series following Pradipta et al. (2015) using a Savitzky-Golay filter of order 7 (future change to this phrase: to do a proper detrending, we should detrend data for a TEC series of a random day when no geomagnetic storm or unusual events happened, callibrate the Savitsky-Golay filter for using a proper order and use it for our data). An example of the resulting detrending signal is shown in figure 2.2. The resulting time series are adequate for wavelet analysis.
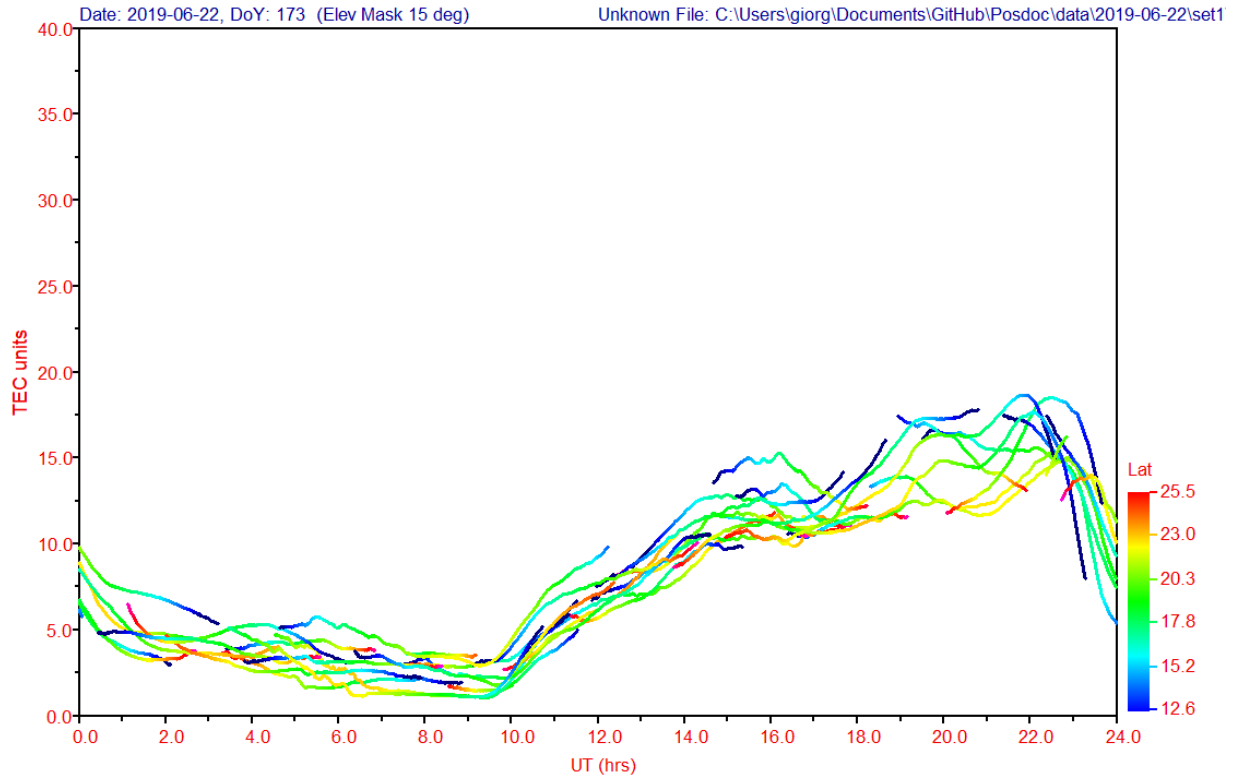
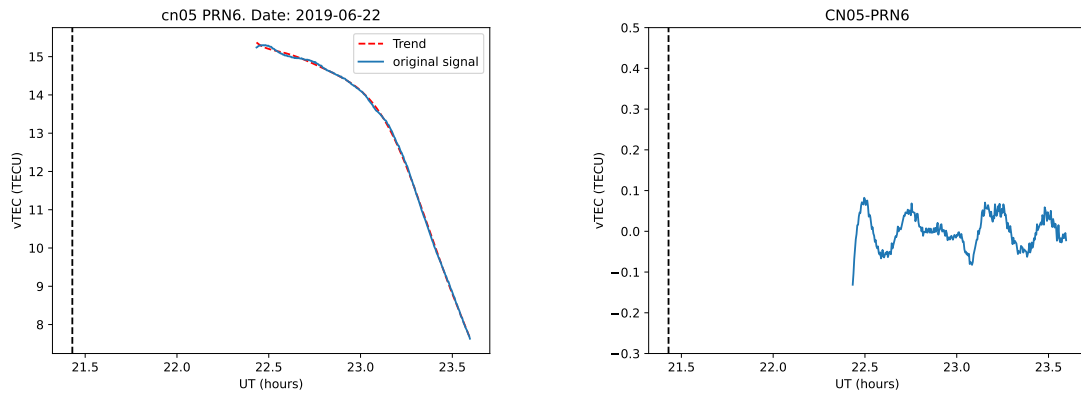Figure 3: Example of TEC curve obtained for GPS data for the bolide USG-09 from CN05 station.

Figure 4: Example of detrending process with USG-09 event. Left: Undetrended TEC series for station CN05 with PRN 6 (blue) versus Golay-Savitsky fit of order 7 (red dashed curve). Right: detrended curve resulting from substracting the Golay-Savitsky fit from the original signal.

2.3 Wavelet analysis

Wavelet analysis is a powerful tool for analyzing variations of power within a time series (Torrence & Compo, 1998). For this task we used a Morlet wavelet $\Psi_0(\eta) = \pi^{-1/4} \exp(i\omega_0\eta) \exp(-\eta^2/2)$, where ω_0 is a non-dimensional frequency, usually set to be 6 to satisfy the admissibity condition (Farge, 1992) and η is a non-dimensional "time parameter".

With this, the wavelet transform is given by:

$$W_n(s) = \sum_{k=0}^{N-1} \hat{x}_k \hat{\Psi}^* (s\omega_k) \exp(i\omega_k n\delta t) \tag{5}$$

Where the $*$ indicates the complex conjugate, $k = 0, 1, \ldots, N-1$ is the frequency index, s is the scale, δt is the time spacing between data, ω_k is the angular frequency defined as:

$$\omega_k = \left\{ \begin{array}{lll} \frac{2\pi k}{N\delta t} & : & k \leq \frac{N}{2} \\ -\frac{2\pi k}{N\delta t} & : & k > \frac{N}{2} \end{array} \right. \tag{6}$$

And $\hat{\Psi}^* (s\omega_k)$ is the normalized wavelet function:

$$\hat{\Psi}^* (s\omega_k) = \left(\frac{2\pi s}{\delta t}\right)^{1/2} \hat{\Psi}_0 (s\omega_k) \tag{7}$$

Since $\Psi(\eta)$ is a complex function, is expected that $W_n(s)$ is also complex. The transform can be divided into real and imaginary part. From the amplitude $|W_n(s)|$, from which we can obtain the power spectrum $|W_n(s)|^2$.

If two stations show similar power spectrums, we can be confident enough to compute the wavelet coherence of both time series, defined as (Yang et al., 2011):

$$R_{1,2}^2 = \frac{|W_{12}|^2}{(|W_1|^2|W_2|^2)} \tag{8}$$

where the $W_{12} = W_1 W_2^*$ is the cross wavelet spectrum, W_i is the wavelet transform of the time series and W_i^* is the complex conjugate of W_i. Regions with high coherence indicate the precence of a TID with frequency $1/T$, where T is the period of the region with high frequency.

3 Bolides physical parameters

Once the estimated the bolides energy, we are capable to estimate other bolides parameters, such as the mass. For that we used a Fragment Cloud Model (Wheeler et al., 2017). To obtain the bolide mass, we must have previous knowledge of its velocity. Based on the few events of the USG sample where we could extract the velocity (see table 2), we tried three models of bolides mass as a function of its releasing energy: the low velocity model, which assumes
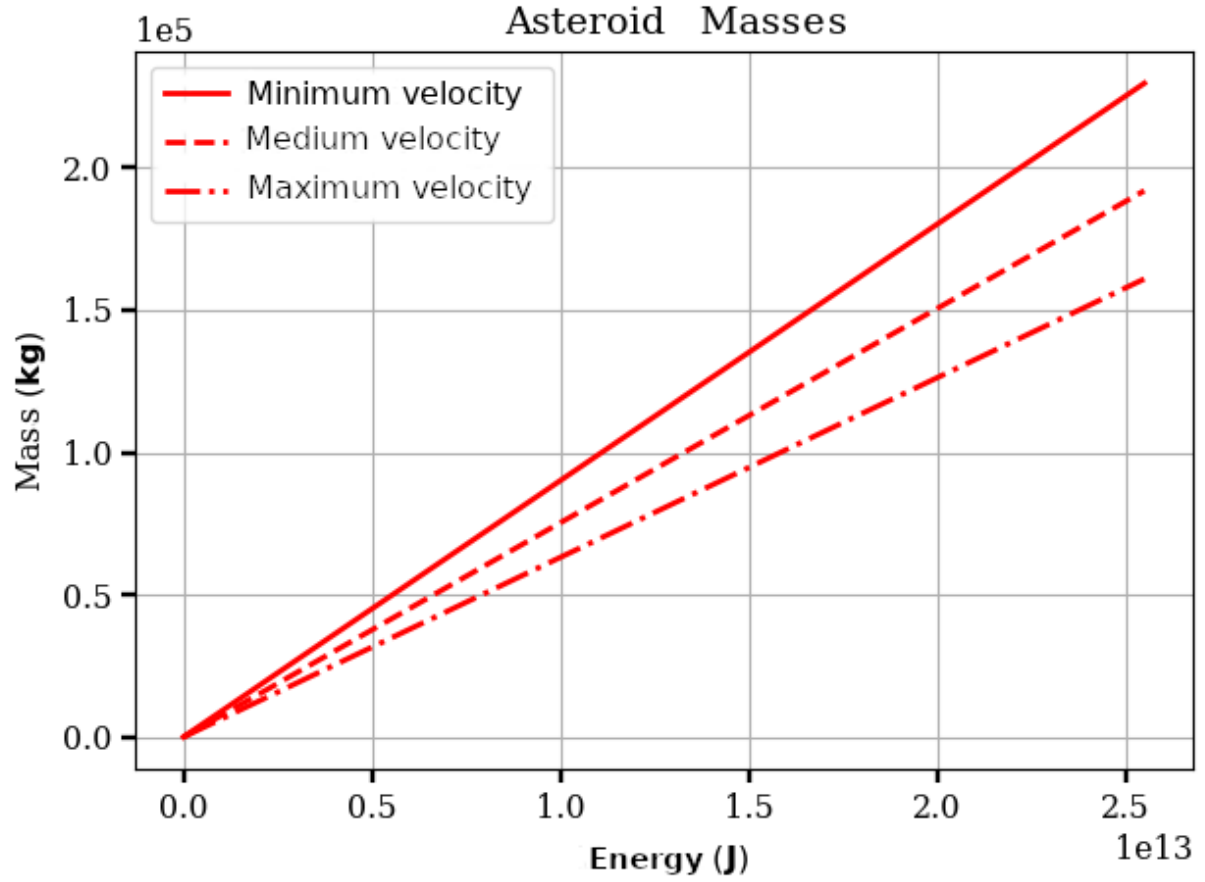
Figure 5: Bolides mass derived from Fragment Cloud Model. We used three assumptions about the bolide velocity: Minimum velocity ($\sim 15\,\mathrm{km\,s^{-1}}$), Medium velocity ($\sim 16\,\mathrm{km\,s^{-1}}$) and maximum velocity ($\sim 18\,\mathrm{km\,s^{-1}}$). This values are based on the available data of USG sample (see table 2)
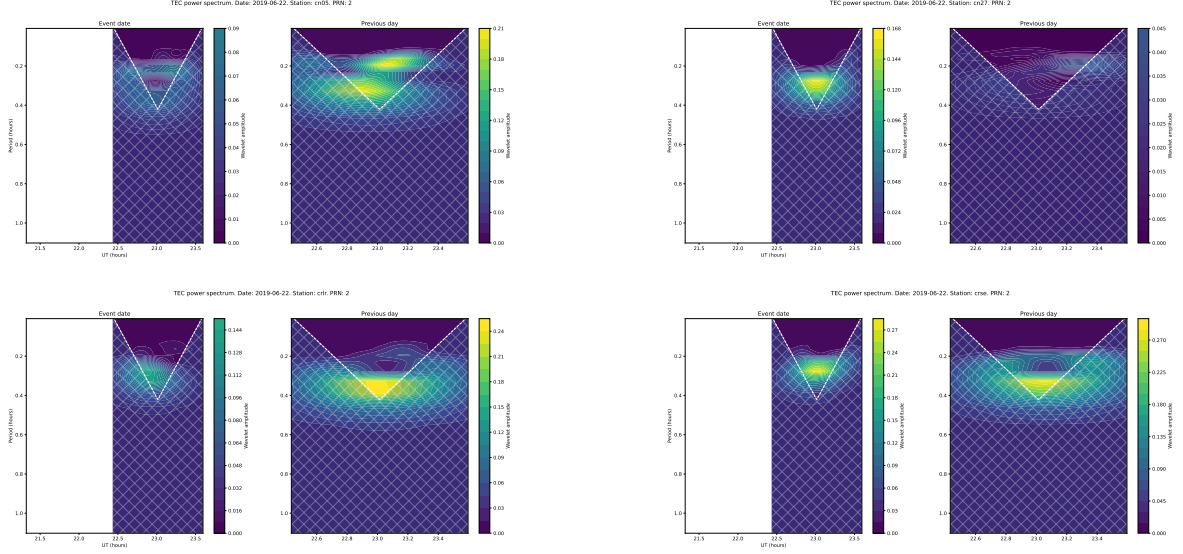
Figure 6: Examples of power spectrums for event USG-09, PRN 2. Top left: Station CN05. Top Right: Station CN27. Bottom left: station CRLR. Bottom right: station CRSE. In each figure the left panel corresponds to the event day and the right panel corresponds to the previous day of the event. The white dashed lines correspond to the Cone of Influence, where all the wavelet spectrum below is subject to error.

a velocity of $\sim 15\,\mathrm{km\,s^{-}}1$, medium velocty $v \sim 16\,\mathrm{km\,s^{-}}1$ and high velocity $v \sim 18\,\mathrm{km\,s^{-}}1$. The resultant masses can be seen in figure 5. For the rest of the sample we need to assume that the bolides velocity is within this range or close enough in order to get a reasonable estimation of its mass.

4 Ionospheric background and wavelet power spectrum

For each TEC series like figure 2.2 we computed $|W_n(s)|^2$ to find any wave-like features in any of the TEC series, where s is the wavelet scale (somehow is the analogous to the wavelength). The presence of this features allow us to trace the TEC perturbations produced by the meteor. Examples are shown in figure 4. Due to the fact we are working with finite time series, edge effects become important at the beginning or the end of the time series, and when the wavelet scale is similar or greater than the time series length. The limit when these errors become important is called Cone of Influence (COI), the COI is shown as a white dashed line in figure 4. At a closer look of this spectra is clear that in some cases the wavelet spectra in the previous day is more intense than the event day. This happens because no TEC perturbations was really detected, but instead noise appears as wavelets. This is an indicator that the TEC perturbances either propagate to other location or it is too faint to be detectable.

5   Discussion and conclusions

We collected data for a sample of meteors which were detected around Mexican territory, or with some exceptions, meteoroids that released enough energy to have a good chance to get a vTEC disturbance with nearby GPS stations. We used data from the GLM, where the total energy was estimated from light curves, and USG sensors, where energy data is available. We used the few events which are present in both samples to re-calibrate the energy obtained for the GLM sample since in this few cases the energy estimated with the GLM data is systematically lower than the energy reported by USG sensors. Using the resulting energies, we estimated the bolides mass using a Fragment Cloud Model assuming a certain velocity range.

We have collected GPS data of nearby stations where the event was detected at the date each event occured, and one day before as comparison. We obtained the the vTEC series and we detrended them to remove the effects of Earth rotation and solar activity and make the wave-like features more evident. With these data, we used a wavelet transform using a Morlet wavelet to discover the frequencies at which vTEC perturbations may be produced, how intense these perturbations are and the time interval of these perturbations. If two different stations detect perturbations at the same frequencies that means that a vTEC perturbation was detected with such stations. We have observed that the distribution of wavelet coherent signal show us that the propagation of ionospheric disturbances have a time intervals of occurrence of a two hours from the spectrograms.

6   Acknowledgments

A   Estimation of distances to meteors

The distance between the GOES satellite and the meteor, neccesary to estimate the radiated energy is calculated as follows:

$$R = |\vec{r}_{GLM} - \vec{r}_{obj}| \tag{9}$$

where $\vec{r}_{GLM}$ is the vector position of the GLM satellite and $\vec{r}_{obj}$ is the vector position of the meteor.

In cartesian coordinates, the distance R is given by:

$$R = \left((x_{GLM} - x_{obj})^2 + (y_{GLM} - y_{obj})^2 + (z_{GLM} - z_{obj})^2\right)^{1/2} \tag{10}$$

$$\tag{11}$$

The transformation to spherical coordinates is given by:

$$x = r\cos\phi\cos\theta \tag{12}$$
$$y = r\sin\phi\cos\theta \tag{13}$$
$$z = r\sin\theta \tag{14}$$

Where r is measured from the center of the earth, $-180° < \phi <= 180°$ represents the longitude; is positive at east of Greenwich meridian, and negative eastwards. $90° <= \theta <= 90°$ represents the latitude and is positive at the north of equator and negative southwards.

Substituting the transform (12 - 14) into (10), using elemental trigonometry and considering both GLM satellites lie into the equator ($\theta_{GLM} = 0$) we get:

$$R^2 = r_{GLM}^2 + r_{obj}^2 - 2r_{GLM}r_{obj}f(\theta_{obj}, \phi_{obj}, \phi_{GLM}) \tag{15}$$
$$\text{where :} f(\theta_{obj}, \phi_{obj}, \phi_{GLM}) = \cos\theta_{obj}\cos(\phi_{GLM} - \phi_{obj}) \tag{16}$$

Since r_{GLM} and r_{obj} are measured from the center of the earth we find that:

$$r_{GLM} = r_{earth} + h_{GLM} \tag{17}$$
$$r_{obj} = r_{earth} + h_{obj} \tag{18}$$

Substituting (17, 18) into 15 and considering that $h_{obj} \ll h_{GLM}$ we get:

$$R^2 = 2r_{earth}^2\left(1 - f(\theta_{obj}, \phi_{obj}, \phi_{GLM})\right) + 2r_{earth}h_{GLM}$$
$$(1 - f(\theta_{obj}, \phi_{obj}, \phi_{GLM})) + h_{GLM}^2 - 2h_{GLM}h_{obj}f(\theta_{obj}, \phi_{obj}, \phi_{GLM}) \tag{19}$$

B   Energy estimation

The total radiant energy emmited is calculated integrating over all the time and all directions. The first is obtained simply summing all the light curve points. In the other hand, to integrate over all directions, we multiply the GLM event energies by the factor $(1.695 \times 10^{18})(1.018 \times 10^3)\left(\frac{R}{35780\ km}\right)^2$ (Jenniskens et al., 2018). This factor also considers that the GLM only detects light from the OI line. Then, we obtain the luminous efficiency τ_1 (i.e the fraction of the total energy converted into radiation) following Brown et al. (2002):

$$\tau_1 = (0.1212 \pm 0.0043)E_0^{0.115 \pm 0.075} \tag{20}$$

Where E_0 is the luminous energy calculated from integrating GLM reported energies (in kilotons). Finally the total estimated energy is $E = E_0/\tau_1$. We may compare the resulting
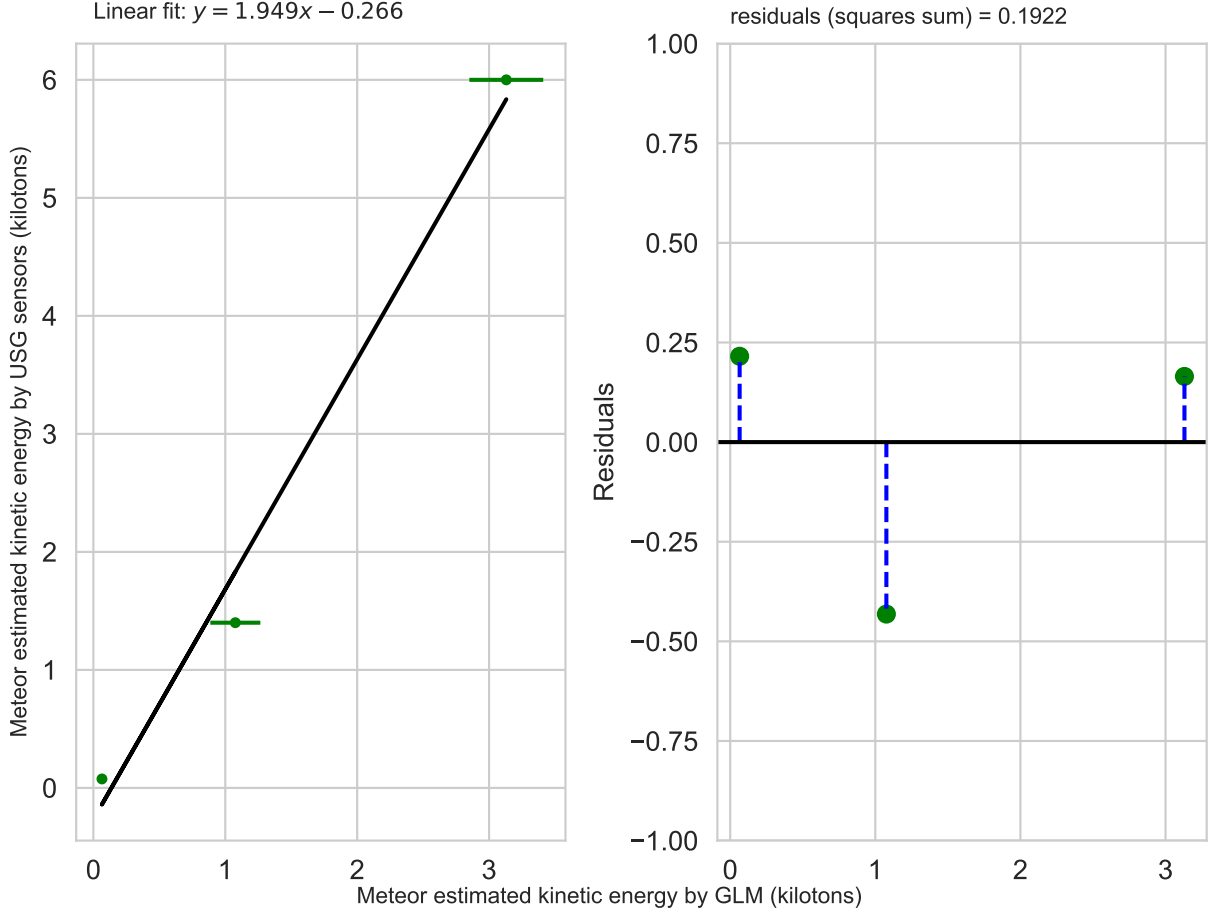
Figure 7: Left: Linear fit between energies calculated from GLM data and energies reported by USG sensors. Right: Residuals of the fit, used as error in the recallibration factor. The three events used for this linear fit are GLM-00 (the cuban meteoroid), GLM-23 and GLM-Ven (Venezolan meteoroid).

GLM energies with the energies reported by USG sensors using the events which belong to both samples, and we noticed that the energies obtained with GLM data is systematically lower than the energies reported by the USG sensors. In this work we assumed that this discrepancy is due to the GLM sensors does not detect the full meteor paths, just a fraction of the total radiated energy. To solve this problem we made a linear fit between the derived energies and the energies reported in the USG sample for the events which appear in both samples, and recallibrate the energies of the rest of the GLM sample. The linear fit is shown in figure 7. We used the linear fit slope as the recallibration factor and the residuals as the error, we neglected the y-intercept term because this term is much larger than the most energies in the GLM sample and strongly affects the recallibrated energy.

References

Blanco-Cano X., Omidi N., Russel C. T., 2004, Astronomy & Geophysics, 45, 3.14

Brown P., Spalding R. E., ReVelle D. O., Tagliaferri E., Worden S. P., 2002, Nature, 420, 294

Chilcote M., LaBelle J., Lind F. D., Coster A. J., Miller E. S., Galkin I. A., Weatherwax A. T., 2015, Radio Science, 50, 249

Cnossen I., Wiltberger M., Ouellette J. E., 2012, Journal of Geophysical Research: Space Physics, 117

Emery W., Camps A., 2017, in Emery W., Camps A., eds, , Introduction to Satellite Remote Sensing. Elsevier, p. 455–564, doi:10.1016/B978-0-12-809254-5.00006-3

Farge M., 1992, Annual Review of Fluid Mechanics, 24, 395

Goodman S. J., et al., 2013, Atmospheric Research, 125-126, 34

Helmboldt J. F., Lane W. M., Cotton W. D., 2012, Radio Science, 47

Jenniskens P., et al., 2018, Meteoritics & Planetary Science, 53, 2445

Kumar D. S., Priyadarshi S., Seemala G., Singh A., 2012, Astrophysics and Space Science, 339, 165

Lin C. H., et al., 2014, Annales Geophysicae, 32, 1145

Oka M., et al., 2011, Geophysical Research Letters, 38

Pradipta R., Valladares C. E., Doherty P. H., 2015, Journal of Geophysical Research: Space Physics, 120, 11,048

Rodríguez-Martínez M., Pérez-Enríquez H. R., Carrillo-Vargas A., López-Montes R., Araujo-Pradere E. A., Casillas-Pérez G. A., Cruz-Abeyro J. A. L., 2014, Sol Phys, 289, 2677

Rumpf C. M., Longenbaugh R. S., Henze C. E., Chavez J. C., Mathias D. L., 2019, Sensors, 19

Sergeeva M. A., et al., 2021, Atmosphere, 12

Torrence C., Compo G. P., 1998, Bulletin of the American Meteorological Society, 79, 61

Vázquez M., Vaquero J. M., Gallego M. C., Roca Cortés T., Pallé P. L., 2016, Sol Phys, 291, 613

Vlasov M. N., Kelley M. C., 2010, Journal of Geophysical Research: Space Physics, 115

Wheeler L. F., Register P. J., Mathias D. L., 2017, Icarus, 295, 149

Yang Y.-M., Garrison J. L., Lee S.-C., 2011, in 2011 IEEE International Geoscience and Remote Sensing Symposium. pp 1131–1134, doi:10.1109/IGARSS.2011.6049396

Yang Y.-M., Komjathy A., Langley R. B., Vergados P., Butala M. D., Mannucci A. J., 2014, Radio Science, 49, 341

Zolesi B., Cander L. R., 2014, Ionospheric Prediction and Forecasting. Springer Geophysics